

Tunable spin-polarized correlated states in twisted double bilayer graphene



<https://doi.org/10.1038/s41586-020-2458-7>

Received: 25 March 2019

Accepted: 19 May 2020

Published online: 8 July 2020

 Check for updates

Xiaomeng Liu^{1,3}, Zeyu Hao¹, Eslam Khalaf¹, Jong Yeon Lee¹, Yuval Ronen¹, Hyobin Yoo¹, Danial Haei Najafabadi¹, Kenji Watanabe², Takashi Taniguchi², Ashvin Vishwanath¹ & Philip Kim¹


Reducing the energy bandwidth of electrons in a lattice below the long-range Coulomb interaction energy promotes correlation effects. Moiré superlattices—which are created by stacking van der Waals heterostructures with a controlled twist angle^{1–3}—enable the engineering of electron band structure. Exotic quantum phases can emerge in an engineered moiré flat band. The recent discovery of correlated insulator states, superconductivity and the quantum anomalous Hall effect in the flat band of magic-angle twisted bilayer graphene^{4–8} has sparked the exploration of correlated electron states in other moiré systems^{9–11}. The electronic properties of van der Waals moiré superlattices can further be tuned by adjusting the interlayer coupling⁶ or the band structure of constituent layers⁹. Here, using van der Waals heterostructures of twisted double bilayer graphene (TDBG), we demonstrate a flat electron band that is tunable by perpendicular electric fields in a range of twist angles. Similarly to magic-angle twisted bilayer graphene, TDBG shows energy gaps at the half- and quarter-filled flat bands, indicating the emergence of correlated insulator states. We find that the gaps of these insulator states increase with in-plane magnetic field, suggesting a ferromagnetic order. On doping the half-filled insulator, a sudden drop in resistivity is observed with decreasing temperature. This critical behaviour is confined to a small area in the density–electric-field plane, and is attributed to a phase transition from a normal metal to a spin-polarized correlated state. The discovery of spin-polarized correlated states in electric-field-tunable TDBG provides a new route to engineering interaction-driven quantum phases.

Moiré superlattices of two-dimensional (2D) van der Waals (vdW) materials provide a new scheme for creating correlated electronic states. By controlling the twist angle θ between atomically thin vdW layers, the size of the moiré unit cell can be tuned^{1–3}. In particular, in twisted bilayer graphene (TBG), the weak interlayer coupling can open up energy gaps at the boundary of the mini-Brillouin zone, which modifies the energy bands of the coupled system. Theoretically, it has been predicted that around $\theta \approx 1.1^\circ$ (the so-called magic angle, MA), the interlayer hybridization induces isolated flat bands with drastically reduced bandwidth and enhanced density of states¹². The combination of flat bands and moiré periodic potential fosters an environment where strongly correlated states can emerge. Recent experiments performed in MA-TBG indeed confirmed the appearance of correlated insulator states associated with the flat bands⁴. Intriguingly, on doping the half-filled insulator, superconductivity was discovered. The phase diagram of MA-TBG thus phenomenologically resembles that of high-temperature superconductors, whose undoped parent compounds are Mott insulators¹³. As a result, there is hope that MA-TBG could be a gateway to understanding the long-lasting puzzle of high-temperature superconductivity.

Yet, in recent studies, the connection between superconductivity and the correlated insulator state has been debated^{14–19}.

One method to study the MA-TBG system is to tune the band structure through the flat-band condition and observe how the correlated physics changes. So far, such experimental control has largely been achieved by fabricating samples with different twist angles. However, different samples—owing to differences in uncontrollable factors such as the alignment with hexagonal boron nitride (hBN), strain and dielectric thickness—often yield contradicting results regarding where the correlated insulator and superconductivity appear. Only limited tunability has been demonstrated in TBG by the application of hydrostatic pressure⁶. In ABC trilayer graphene/hBN superlattices, the electric field has been shown to modulate the correlated insulator gap⁹, opening up the possibility of continuous tuning of the moiré flat band with electric field. However, the difficulty in identifying and preserving the unstable ABC trilayer graphene, together with the precise alignment required between the graphene and hBN layers, makes it a less accessible platform. Here we demonstrate a wide range of electric field tunability in the moiré flat band of twisted double bilayer graphene (TDBG),

¹Department of Physics, Harvard University, Cambridge, MA, USA. ²National Institute for Material Science, Tsukuba, Japan. ³These authors contributed equally: Xiaomeng Liu, Zeyu Hao.

 e-mail: xiaomeng@princeton.edu; pkim@physics.harvard.edu

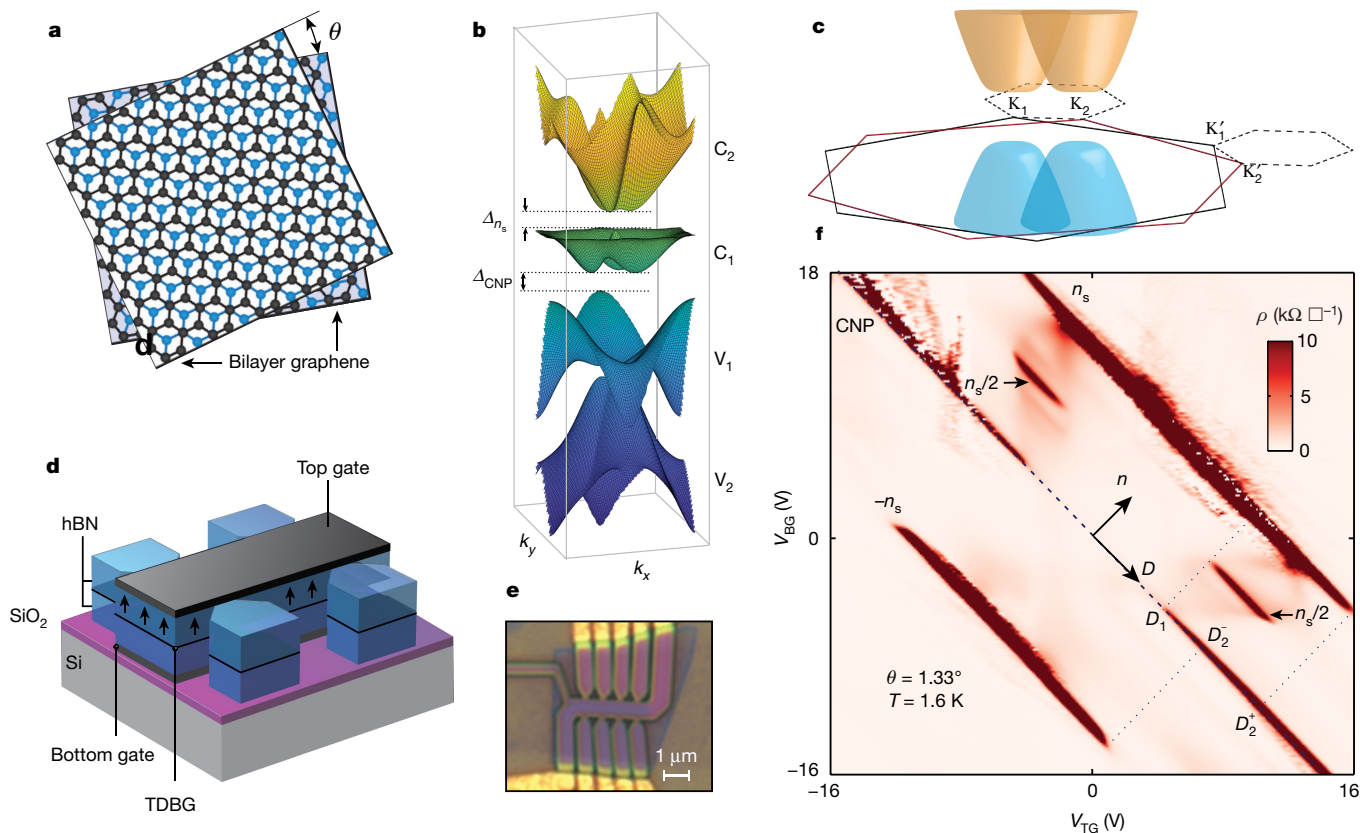


Fig. 1 | Band structure and insulating states in the $\theta = 1.33^\circ$ sample. **a**, Schematic of TDBG with a twist angle θ . **b**, Calculated band structure for $\theta = 1.33^\circ$ TDBG at an optimal displacement field. k_x and k_y are wave vectors in the x and y direction. **c**, Brillouin zone and band structure of the two individual bilayer graphene layers under a perpendicular displacement field. The dashed hexagons represent the mini-Brillouin zone of the moiré superlattice. K_1 and K'_1 (K_2 and K'_2) are the two valleys of the top (bottom) bilayer graphene. **d**, Device

consisting of two Bernal-stacked bilayer graphene sheets misaligned with a twist angle θ (Fig. 1a).

In twisted systems, the twist angle for achieving a flat band is determined by the band structure of the individual layer and the interlayer coupling strength. Unlike monolayer graphene, the band structure of Bernal-stacked bilayer graphene can be tuned by a perpendicular displacement field D (ref. 20). As $|D|$ increases, the parabolic band touching at charge neutrality of bilayer graphene opens up a gap and the bottom (top) of the conduction (valence) band lifts up (down) into a shallow Mexican-hat-shaped energy dispersion distorted by trigonal warping²¹. The gap in bilayer graphene can be as large as 200 meV for large $|D|$ before the gate dielectric breaks down²². In TDBG, where two bilayers are stacked, the displacement field affects the energy dispersion of each constituent bilayer graphene, allowing a new experimental ‘knob’ to tune the flat-band condition (Fig. 1c). Figure 1b shows moiré band structures calculated at finite D using the single-particle continuum model approximation^{12,23–27}. We find that a well-isolated narrow conduction band can appear for a range of twist angles θ , where the interband energy gaps and bandwidth can be controlled by the displacement field (see Methods for details).

We fabricated TDBG devices by tearing and stacking Bernal-stacked bilayer graphene^{28,29}. We measured in total seven devices with twist angle $\theta = 1.26, 1.32, 1.33, 1.41, 1.48, 1.53$ and 2.00° , with the first six devices showing signatures of correlation effects. All of the devices measured are encapsulated by hBN. Top gates are made from graphite or metal, and bottom gates are made from graphite or silicon (details for each device structure are shown in Extended Data Fig. 9). We focus

our study on the two representative devices $\theta = 1.33^\circ$ and $\theta = 1.26^\circ$, and summarize the behaviour of the other devices in Methods and Extended Data Table 1. The top and bottom gates with voltages V_{TG} and V_{BG} are used to control the density of electrons, n , and displacement field, D , independently: $n = (C_{TG}V_{TG} + C_{BG}V_{BG})/e$ and $D = (C_{TG}V_{TG} - C_{BG}V_{BG})/2$, where C_{TG} (C_{BG}) is the capacitance between the TDBG and the top (bottom) gate and e is the elementary charge.

Figure 1f shows the four-probe resistivity ρ measured in the TDBG with $\theta = 1.33^\circ$ as a function of V_{TG} and V_{BG} at temperature $T = 1.6$ K. CNP represents the charge neutral point of the TDBG and n_s denotes the full filling of the flat band, corresponding to four electrons per moiré unit cell, originating from the spin and valley degeneracy. For a linecut along a constant displacement field $D \approx (D_1 + D_2^-)/2$ (the positions of D_1 and D_2^\pm are labelled in Fig. 1f), ρ shows several insulating states where the corresponding conductance $\sigma = \rho^{-1}$ vanishes as the temperature T decreases (Fig. 2a), suggesting a gap opening at the Fermi level of the system. Some insulating regions identified in Fig. 1f can be well explained by the single-particle band structure presented in Fig. 1b. For example, we find that the CNP is gapless at $D = 0$ but develops a gap for $|D| > D_1 \neq 0$. Similarly, at full moiré band filling $n = \pm n_s$, energy gaps $\Delta_{\pm n_s}$ are present within displacement field ranges $|D| < D_2^\pm$. Consequently, for $D_1 < |D| < D_2^+$ ($D_1 < |D| < D_2^-$), there is an isolated conduction (valence) band. Note that D_2^\pm is different in the conduction band (+) and valence band (–), owing to the lack of electron–hole symmetry in TDBG. All these single-particle bandgaps are nicely captured by our calculation based on a continuum model (Extended Data Fig. 1). The calculation also captures the cross-like feature in Fig. 1f, which matches with the

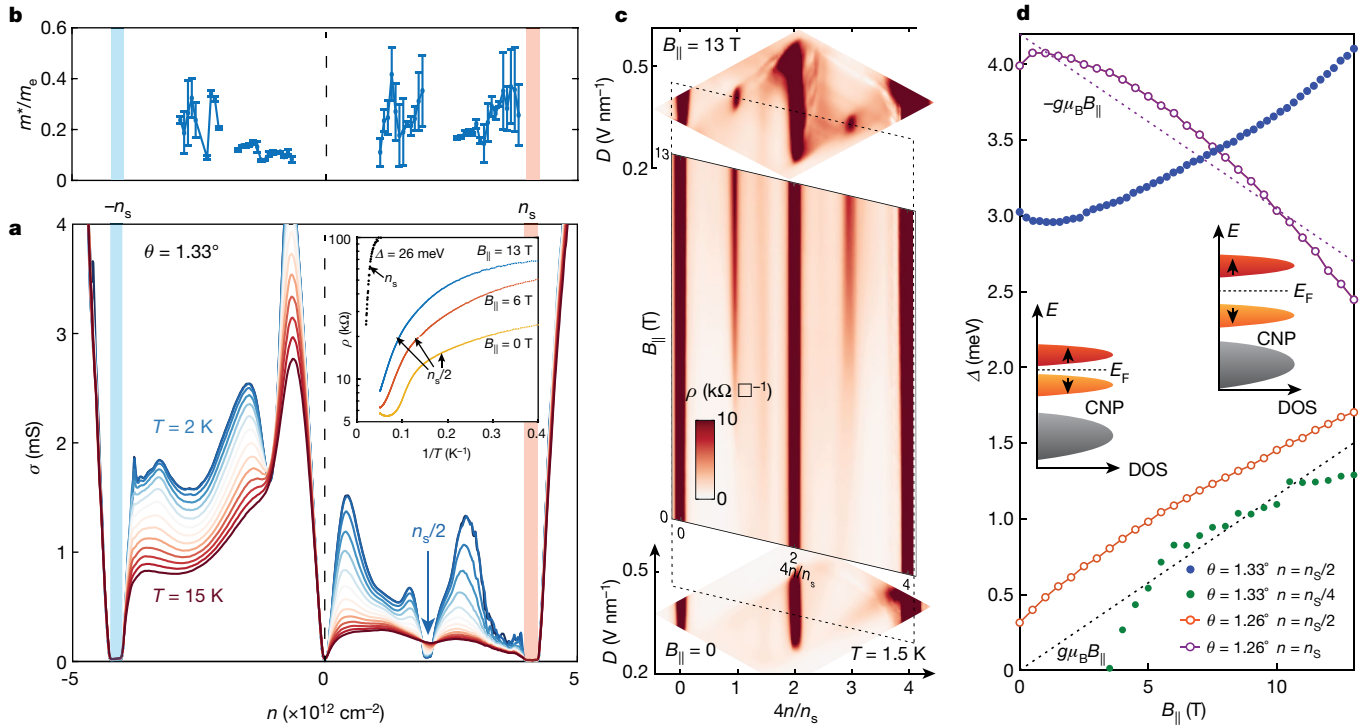


Fig. 2 | Spin polarization of the correlated insulator states. **a**, Temperature dependence of conductivity (σ) as a function of carrier density at a constant displacement field that passes through the half-filled insulator ($D \approx (D_1 + D_2)/2$). Inset: Arrhenius plot for the full-filled insulating state (n_s) and the half-filled insulating state ($n_s/2$) under different in-plane magnetic fields. **b**, Effective mass measured by temperature-dependent quantum oscillations corresponding to **a**. **c**, Development of the correlated insulating states with in-plane magnetic fields. Top and bottom panels compare resistivity as a function of n and D under in-plane magnetic fields of $B_{||} = 0$ T (bottom) and $B_{||} = 13$ T (top). The middle panel shows the continuous evolution of the correlated states by taking a linecut along the dashed lines in the top and

bottom panels. All three panels are measured at a temperature of $T = 1.5$ K. **d**, Half-filled insulating gap $\Delta_{n_s/2}$, quarter-filled insulating gap $\Delta_{n_s/4}$ and full-filled gap Δ_{n_s} as a function of in-plane magnetic field. The black dashed line indicates Zeeman energy with $g = 2$. $\Delta_{n_s/2}$ of both devices increases with in-plane magnetic field, indicating spin polarization of the half-filled insulator. We also note that the single-particle gap Δ_{n_s} between c_1 and c_2 (purple curve) decreases linearly with Zeeman energy with a g -factor of 2 (purple dashed line). Inset: schematic of the half-filled insulating state at zero (left) and large (right) in-plane fields. The x axis is density of state (DOS) and the y axis is energy (E_F is the Fermi energy). Grey represents the inert valence band while orange (red) represents the lower (upper) half of the first conduction band.

van Hove singularities of the bands (details in Methods). Lastly, the calculated band structure (Fig. 1b) indeed demonstrates the existence of an isolated flat band at $\theta = 1.33^\circ$ under finite displacement field with a bandwidth around 10–15 meV.

In this single-particle band structure, we expect a narrow but uninterrupted spectrum within the lowest moiré conduction band (c_1), separated by bandgaps from both the valence band (v_1) and higher conduction band (c_2) for $D_1 < |D| < D_2$. However, we observe the development of a well-defined insulating behaviour at half-filling $n = n_s/2$ (Figs. 1f, 2a). The onset displacement field of this insulating state coincides with D_1 . However, it ends well before D reaches D_2^+ , suggesting both the isolation and the flatness of the band are required for creating the observed correlated gap (Fig. 1f). Along the same linecut shown in Fig. 2a ($D \approx (D_1 + D_2)/2$), we measure the effective cyclotron mass m^* from the temperature-dependent magnetoresistance oscillations (Extended Data Fig. 8). Figure 2b shows that $m^* \approx 0.2m_e$ for the first valence band (v_1) and $m^* \approx 0.3m_e$ for the first conduction band (c_1), where m_e is the bare electron mass. Considering the effective mass of Bernal-stacked bilayer graphene is about $0.04m_e$ (ref. ³⁰), the experimentally observed large m^* indicates an order of magnitude narrower bandwidth than that of bilayer graphene bands folded in the moiré superlattice Brillouin zone, especially for the c_1 band. We then use the conduction band effective mass $m^* = 0.3m_e$ to estimate the bandwidth of the c_1 band to be about 10 meV. This bandwidth matches with the continuum model calculation of TDBG²³, confirming the existence of the flat band experimentally. The absence of correlated insulating behaviour in the hole-doped regime under similar experimental

conditions can be explained by the larger bandwidth of the moiré valence band v_1 than that of c_1 (Methods).

We measure the size of the insulating gaps from the activating behaviour of ρ (Fig. 2a, inset). For $\theta = 1.33^\circ$ TDBG, the half-filled insulator is robust with an energy gap of $\Delta_{n_s/2} = 3$ meV and persists up to a perpendicular magnetic field $B_\perp \approx 7$ T (Extended Data Fig. 7). As the c_1 band is spin and valley degenerate in a single-particle picture, the half-filled insulator is probably polarized in the fourfold spin–valley space. The in-plane magnetic field $B_{||}$ can be used to probe the spin structure of the state without substantially coupling to the valley degrees of freedom in the regime where in-plane orbital effect is negligible. In MA-TBG, it has been shown that $B_{||}$ reduces $\Delta_{n_s/2}$. Figure 2a inset and Fig. 2c show the change of ρ as a function of $B_{||}$ in our TDBG sample. We find that the half-filled insulator becomes more insulating as $B_{||}$ increases (Fig. 2a, inset) and the displacement field range spanned by the half-filled insulator expands (Fig. 2c). More quantitatively, we find that the growth of $\Delta_{n_s/2}$ roughly follows the Zeeman energy scale $g\mu_B B_{||}$, where μ_B is the Bohr magneton and the effective g -factor $g = 2$ (dashed black line in Fig. 2d). This observation is consistent with a picture where the occupied states (half of the states in c_1) are spin polarized along the direction of the external magnetic field. The unoccupied excited states then carry the opposite spin, separated by a ferromagnetic gap due to spontaneous symmetry breaking at half-filling. For spin-1/2, the Zeeman term lowers the energy of the filled states $\Delta E_\downarrow = -g\mu_B B/2$, while boosting the energy of the empty states with opposite spins by $\Delta E_\uparrow = g\mu_B B/2$, pushing the two bands further apart and enhancing the gap (as illustrated by Fig. 2d, insets). Calculations from the Hartree–Fock

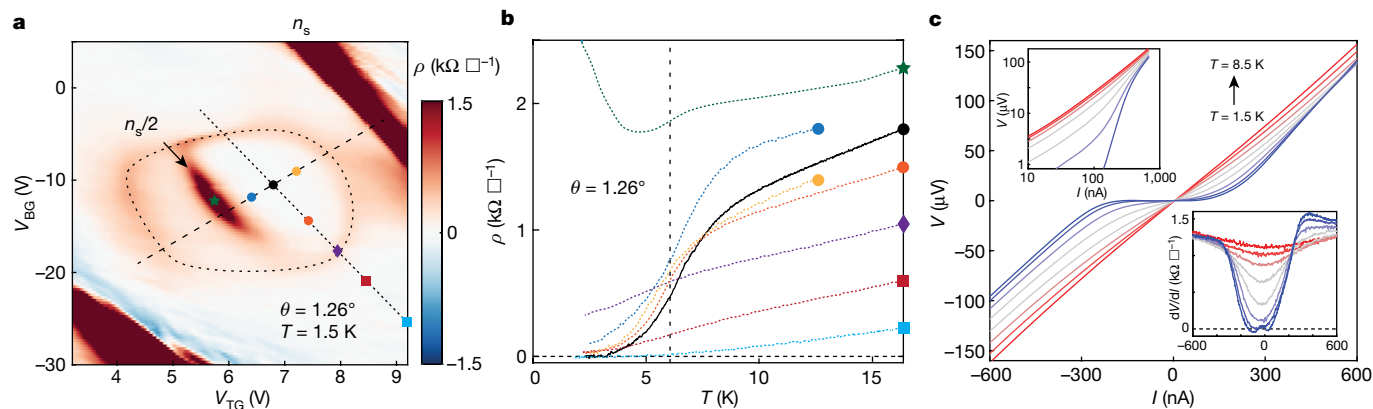


Fig. 3 | Critical transition behaviour in the $\theta = 1.26^\circ$ sample. a, Resistivity map around the half-filled insulator. Dashed circle marks the halo. **b**, Resistivity as a function of temperature at different spots marked by the coloured symbols in **a** using the corresponding colours and shapes. **c**, I - V curves at the black circle

approximation also support the existence of a spin-polarized correlated insulating state at half-filling in TDBG^{23,24}.

In the $\theta = 1.33^\circ$ device, applying B_{\parallel} also induces additional correlated insulating states at quarter-filling ($n = \frac{1}{4}n_s$) and three-quarter-filling ($n = \frac{3}{4}n_s$) (Fig. 2c). The quarter-filled insulating gap opens at $B_{\parallel} \approx 4$ T and increases as B_{\parallel} increases (Fig. 2d). According to the hierarchy of the symmetry-broken states within mean-field theory²³, the quarter-filled gaps separate the ground state and the excited state of the same spin and opposite valleys, and thus should be relatively insensitive to in-plane magnetic fields. However, the enhancement of quarter-filled gaps with B_{\parallel} and the positions where quarter-filled insulating states appear in the n - D plane (Extended Data Fig. 2) suggest that these gaps probably separate states of opposite spin, hinting that the origin of these strongly correlated states goes beyond a simple mean-field approach.

In the $\theta = 1.26^\circ$ sample, a similar spin-polarized half-filled insulating state is observed (Fig. 3a), with a much smaller correlated gap $\Delta_{n_s/2} = 0.3$ meV (red line in Fig. 2d). On doping the half-filled insulator, we identify the appearance of a ‘halo’ (marked with a dashed circle in Fig. 3a) surrounding the half-filled insulating state in the V_{TG} - V_{BG} plane. On the halo, the resistivity is slightly higher than that of the nearby region. Such a halo-like feature commonly appears around the correlated insulating states in different samples with varying twist angles (Fig. 4a–d, Extended Data Fig. 9). The half-filled insulating state divides the halo-like region into two. For the samples with a strong half-filled insulating gap, Hall measurements performed at low magnetic fields (Extended Data Fig. 2) show a sign change of the Hall signal across the boundary of the halo and also across the correlated insulator. A similar observation has been noted in a recent related study³¹. The sign of the Hall signal inside the halo complies with the carrier concentration counted from half-filling. This suggests the metallic state in the halo is obtained by adding carriers to the spin-polarized band at half-filling while retaining the spin-splitting of the band (Fig. 2d, inset), and therefore is probably a ferromagnetic metal. As the Hall signal outside the halo matches the expectation for a moiré band without correlation, the halo marks the border between the spin-polarized and the spin-unpolarized metallic states (Extended Data Fig. 2c).

Studying the temperature dependence of the resistivity, $\rho(T)$, inside the halo, we identify a critical transition with a sudden drop in resistivity as the temperature decreases. Figure 3b shows the resistivity measured at different gate configurations marked by matching symbols in Fig. 3a. We note that the critical transition behaviour, namely the sudden drop in resistivity, occurs only inside the halo. In contrast, resistivity outside the halo increases linearly with temperature. The resistivity

in **a**. Top left inset: I - V on a logarithmic scale, demonstrating the BKT-like power-law behaviour (see Extended Data Fig. 4 for more details). Bottom right inset: dV/dI as a function of bias current, which shows a critical current of about 300 nA. The curves cover temperature from 1.5 K (blue) to 8.5 K (red).

behaviour outside the halo is most likely due to ballistic transport at low temperatures and enhanced phonon scattering at elevated temperatures. The critical transition behaviour of $\rho(T)$ inside the halo, however, appears non-trivial. The $\rho(T)$ curve of the 1.26° device (black curve in Fig. 3b) in particular strongly resembles that of a superconductor, with near-zero resistivity below 3.5 K. The current–voltage (I - V) curve also shows superconducting-like nonlinear behaviours: dV/dI vanishes for bias current smaller than the critical current, $I < I_c$, and increases to a near-constant value that is close to the normal resistivity above the critical transition for $I > I_c$ (Fig. 3c, bottom right inset). This nonlinear I - V characteristic is distinct from that of a heating effect (see Methods for a more detailed analysis) and seemingly follows that of the Berezinskii–Kosterlitz–Thouless (BKT) transition (Extended Data Fig. 4e).

While $\rho(T)$ and the I - V characteristic discussed above for the 1.26° device are suggestive of superconductivity, we note that several factors require careful consideration. First, we have not observed direct evidence of superconducting phase coherence, such as the Fraunhofer pattern under magnetic fields. Second, $\rho(T \ll T_c) \approx 0$ has been observed only for the 1.26° device. Figure 4a–d shows four other devices we measured with the twist angle ranging between 1.32° and 1.48° . In these devices, similar to the 1.26° device, critical transition behaviours in the $\rho(T)$ curves are commonly observed inside the halo region that surrounds the half-filled insulator. These critical behaviours are best illustrated by the clear peaks in $d\rho/dT$, which are absent outside the halo (Fig. 4e, f). The critical temperatures, defined as the temperature where $d\rho/dT$ is maximum, are similar across all devices ($T_c = 6$ – 9 K), despite their very different half-filled insulating gap sizes (Extended Data Table 1). However, the low-temperature resistivity $\rho(T \ll T_c)$ does not reach zero, unlike in the 1.26° device (Fig. 4e, Extended Data Table 1). Strong nonlinear I - V at low temperatures is also absent in these devices.

On the basis of these experimental findings, we propose a few scenarios to explain the observed critical transition behaviour. One possibility is that the critical transition is a result of Cooper-pair formation, but superconductivity is developed only in the 1.26° device. In other devices, the establishment of phase coherence may be inhibited by an inhomogeneous distribution of strains or disorder. Alternatively, the critical transition may correspond to a ferromagnetic transition of the doped half-filled insulating states. Here we note that the critical transition behaviours occur only inside the halo region, which we associate with ferromagnetic metallic states. As the temperature increases, the ferromagnetic metal turns into a normal metal when the correlation effect vanishes. Below the critical temperature, carrier scattering processes related to spin-flip can potentially be suppressed by the ferromagnetic order, resulting in a reduced resistivity. These two scenarios

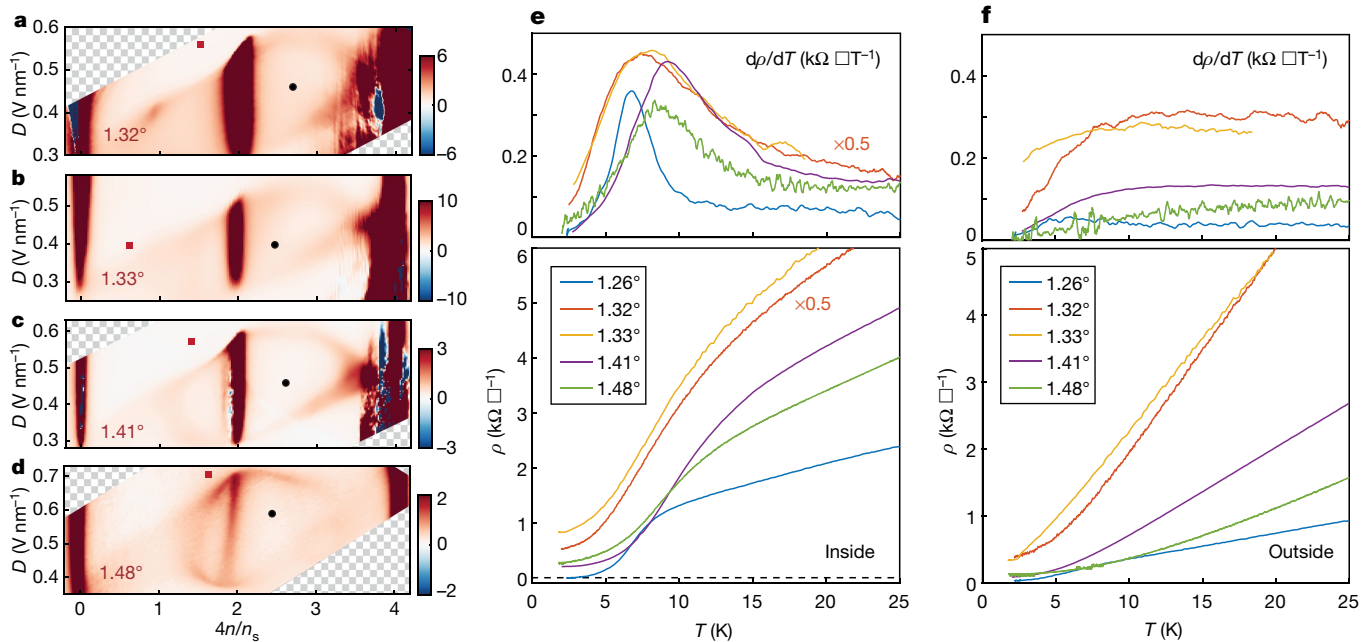


Fig. 4 | Gate-tunable flat band and critical behaviour in a series of twist angles. a–d. Resistivity as a function of filling fraction and displacement field around the half-filled insulators measured in four different samples with twist angles of 1.32° (a), 1.33° (b), 1.41° (c) and 1.48° (d). **e, f.** Resistivity as a function of temperature inside (e) and outside (f) the halo regions surrounding the

correlated insulator. The gate configuration for each curve is marked by the red (outside the halo) and the black (inside the halo) symbols in a–d. Top panels show the derivative of the resistivity to highlight the critical transition behaviour.

do not necessarily compete with each other, leaving open the possibility of a ferromagnetic superconductor (Methods, Extended Data Fig. 5). The highly tunable electronic structures of TDBG demonstrated here and in related studies^{31–34} may provide a new route to engineer correlated phenomena in a moiré superlattice.

Online content

Any methods, additional references, Nature Research reporting summaries, source data, extended data, supplementary information, acknowledgements, peer review information; details of author contributions and competing interests; and statements of data and code availability are available at <https://doi.org/10.1038/s41586-020-2458-7>.

- Dean, C. R. et al. Hofstadter's butterfly and the fractal quantum Hall effect in moiré superlattices. *Nature* **497**, 598–602 (2013).
- Ponomarenko, L. A. et al. Cloning of Dirac fermions in graphene superlattices. *Nature* **497**, 594–597 (2013).
- Hunt, B. et al. Massive Dirac fermions and Hofstadter butterfly in a van der Waals heterostructure. *Science* **340**, 1427–1430 (2013).
- Cao, Y. et al. Correlated insulator behaviour at half-filling in magic-angle graphene superlattices. *Nature* **556**, 80–84 (2018).
- Cao, Y. et al. Unconventional superconductivity in magic-angle graphene superlattices. *Nature* **556**, 43–50 (2018).
- Yankowitz, M. et al. Tuning superconductivity in twisted bilayer graphene. *Science* **363**, 1059–1064 (2019).
- Sharpe, A. L. et al. Emergent ferromagnetism near three-quarters filling in twisted bilayer graphene. *Science* **365**, 605–608 (2019).
- Serlin, M. et al. Intrinsic quantized anomalous Hall effect in a moiré heterostructure. *Science* **367**, 900–903 (2020).
- Chen, G. et al. Evidence of a gate-tunable Mott insulator in a trilayer graphene moiré superlattice. *Nat. Phys.* **15**, 237–241 (2019).
- Wang, L. et al. Magic continuum in twisted bilayer WSe₂. Preprint at <http://arxiv.org/abs/1910.12147> (2019).
- Regan, E. C. et al. Mott and generalized Wigner crystal states in WSe₂/WS₂ moiré superlattices. *Nature* **579**, 359–363 (2020).
- Bistritzer, R. & MacDonald, A. H. Moiré bands in twisted double-layer graphene. *Proc. Natl Acad. Sci. USA* **108**, 12233–12237 (2011).
- Keimer, B., Kivelson, S. A., Norman, M. R., Uchida, S. & Zaanen, J. From quantum matter to high-temperature superconductivity in copper oxides. *Nature* **518**, 179–186 (2015).
- Koshino, M. et al. Maximally localized Wannier orbitals and the extended Hubbard model for twisted bilayer graphene. *Phys. Rev. X* **8**, 031087 (2018).

- Kang, J. & Vafek, O. Symmetry, maximally localized Wannier states, and a low-energy model for twisted bilayer graphene narrow bands. *Phys. Rev. X* **8**, 031088 (2018).
- Po, H. C., Zou, L., Vishwanath, A. & Senthil, T. Origin of Mott insulating behavior and superconductivity in twisted bilayer graphene. *Phys. Rev. X* **8**, 031089 (2018).
- Stepanov, P. et al. The interplay of insulating and superconducting orders in magic-angle graphene bilayers. Preprint at <http://arxiv.org/abs/1911.09198> (2019).
- Saito, Y., Ge, J., Watanabe, K., Taniguchi, T. & Young, A. F. Decoupling superconductivity and correlated insulators in twisted bilayer graphene. Preprint at <http://arxiv.org/abs/1911.13302> (2019).
- Arora, H. S. et al. Superconductivity without insulating states in twisted bilayer graphene stabilized by monolayer WSe₂. Preprint at <http://arxiv.org/abs/2002.03003> (2020).
- Castro Neto, A. H., Guinea, F., Peres, N. M. R., Novoselov, K. S. & Geim, A. K. The electronic properties of graphene. *Rev. Mod. Phys.* **81**, 109–162 (2009).
- McCann, E. & Koshino, M. The electronic properties of bilayer graphene. *Rep. Prog. Phys.* **76**, 056503 (2013).
- Zhang, Y. et al. Direct observation of a widely tunable bandgap in bilayer graphene. *Nature* **459**, 820–823 (2009).
- Lee, J. Y. et al. Theory of correlated insulating behaviour and spin-triplet superconductivity in twisted double bilayer graphene. *Nat. Commun.* **10**, 5333 (2019).
- Zhang, Y.-H., Mao, D., Cao, Y., Jarillo-Herrero, P. & Senthil, T. Nearly flat Chern bands in moiré superlattices. *Phys. Rev. B* **99**, 075127 (2019).
- Koshino, M. Band structure and topological properties of twisted double bilayer graphene. *Phys. Rev. B* **99**, 235406 (2019).
- Chebrolov, N. R., Chittari, B. L. & Jung, J. Flat bands in twisted double bilayer graphene. *Phys. Rev. B* **99**, 235417 (2019).
- Choi, Y. W. & Choi, H. J. Intrinsic band gap and electrically tunable flat bands in twisted double bilayer graphene. *Phys. Rev. B* **100**, 201402 (2019).
- Cao, Y. et al. Superlattice-induced insulating states and valley-protected orbits in twisted bilayer graphene. *Phys. Rev. Lett.* **117**, 116804 (2016).
- Kim, K. et al. van der Waals heterostructures with high accuracy rotational alignment. *Nano Lett.* **16**, 1989–1995 (2016).
- Li, J. et al. Effective mass in bilayer graphene at low carrier densities: the role of potential disorder and electron–electron interaction. *Phys. Rev. B* **94**, 161406 (2016).
- He, M. et al. Tunable correlation-driven symmetry breaking in twisted double bilayer graphene. Preprint at <http://arxiv.org/abs/2002.08904> (2020).
- Shen, C. et al. Correlated states in twisted double bilayer graphene. *Nat. Phys.* **16**, 520–525 (2020).
- Cao, Y. et al. Tunable correlated states and spin-polarized phases in twisted bilayer–bilayer graphene. *Nature* <https://doi.org/10.1038/s41586-020-2260-6> (2020).
- Burg, G. W. et al. Correlated insulating states in twisted double bilayer graphene. *Phys. Rev. Lett.* **123**, 197702 (2019).

Publisher's note Springer Nature remains neutral with regard to jurisdictional claims in published maps and institutional affiliations.

© The Author(s), under exclusive licence to Springer Nature Limited 2020

Band structure of TDBG

The band structure of TDBG with Bernal-stacked bilayers was obtained as follows. In TDBG, each bilayer graphene has a tight-binding Bloch Hamiltonian at a momentum \mathbf{k} given by

$$H(\mathbf{k}) = \begin{pmatrix} U_1 + \Delta & -\gamma_0 f(\mathbf{k}) & \gamma_4 f^*(\mathbf{k}) & \gamma_1 \\ -\gamma_0 f^*(\mathbf{k}) & U_1 & \gamma_3 f(\mathbf{k}) & \gamma_4 f^*(\mathbf{k}) \\ \gamma_4 f(\mathbf{k}) & \gamma_3 f^*(\mathbf{k}) & U_2 & -\gamma_0 f(\mathbf{k}) \\ \gamma_1 & \gamma_4 f(\mathbf{k}) & -\gamma_0 f^*(\mathbf{k}) & U_2 + \Delta \end{pmatrix} \quad (1)$$

which is labelled in the order of A1, B1, A2 and B2 sites of the top (1) and the bottom (2) Bernal stacked bilayer graphene. In function $f(\mathbf{k}) \equiv \sum_l e^{i\mathbf{k} \cdot \delta_l}$, i is the imaginary unit, index l runs from one to three, $\delta_1 = a(0, 1)$, $\delta_2 = a(\sqrt{3}/2, -1/2)$ and $\delta_3 = a(-\sqrt{3}/2, -1/2)$, with $a = 1.42 \text{ \AA}$. $f^*(\mathbf{k})$ is the complex conjugate of $f(\mathbf{k})$. In particular, the electrostatic energy difference U between the top and bottom layers is an important tuning parameter controlled by D . With this Hamiltonian, one can follow the continuum model approach in ref.¹² to calculate the moiré band structure.

In the numerical simulation, we use phenomenological parameters

$$(\gamma_0, \gamma_1, \gamma_3, \gamma_4, \Delta) = (2, 610, 361, 283, 138, -15) \text{ meV} \quad (2)$$

obtained from ref.³⁵. Compared with TBG, TDBG has additional parameters γ_1 and γ_3 (trigonal warping), γ_4 (particle-hole asymmetry) and Δ , in addition to γ_0 (nearest-neighbour hopping). Here, γ_1 and Δ are the interlayer hopping and the on-site energy at A–B stacked sites, where the A site of the first layer (A1) sits on top of the B site of the second layer (B2), respectively. Although these parameters are much smaller than γ_0 , they are important to understand the experimental data. In particular, for vanishing U , a finite value of γ_3 yields a larger bandwidth and overlap between c_1 and v_1 . This is why the system is metallic at the CNP and there is no magic-angle condition at $D = 0$. Furthermore, γ_4 and Δ give rise to the electron–hole asymmetry. Owing to these terms, the bandwidth of v_1 is much larger than that of c_1 , resulting in smaller band isolation for v_1 (Extended Data Fig. 1). For the moiré hopping parameters, $(w_0, w_1) = (0.08, 0.1) \text{ eV}$ is used to account for the relaxation effect described by ref.³⁶. The relaxation increases the gap between c_1 and c_2 (v_1 and v_2), stabilizing the insulating states for the range of D at $n = \pm n_s$ fillings. For more details, see ref.²³.

Extended Data Fig. 1c, d shows a direct comparison between experimental resistivity and the calculated density of states at the Fermi energy for the $\theta = 1.33^\circ$ TDBG. The experimental results are plotted against displacement field D while the calculation is plotted against onset potential difference between the top-most and bottom-most graphene layer U . The conversion between the experimental parameter D and the calculation parameter U is not straightforward owing to the screening of the electric field by the graphene layers themselves. Thus, converting D to U requires a self-consistent calculation of the screening effect produced by the TDBG band structure, which in turn depends on U . However, in Extended Data Fig. 1, we see a very good match between experimental single-particle insulating states and theoretical gaps at the Fermi energy when we convert D into U with an empirical factor: $U = 0.1 \text{ nm} \times eD$, where e is the electron charge. Besides the single-particle gaps, the calculation also shows regions of high density of states. In particular, in experimental data, there are two lines with higher resistivity than the surroundings: from $(n, D) = (-1, -0.2)$ to $(1, 0.6)$ and from $(n, D) = (-1, 0.2)$ to $(1, -0.6)$. These two lines form a cross and pass through the half-filled insulator as well as the halo features. By comparing with the calculation, we recognize that these experimental features correspond to the regions of high density of states shown in Extended Data Fig. 1d.

Hall effect and ferromagnetism phase boundary

In Extended Data Fig. 2, we show the Hall effect measured in the sample with the most robust half-filled insulating states ($\theta = 1.41^\circ$, $\Delta_{n_s/2} = 4.2 \text{ meV}$). There is a clear change in Hall resistance behaviour across the halo boundary, which is identifiable in the longitudinal resistance measurement (Extended Data Fig. 2a). Inside the halo, the Hall resistance changes sign across the half-filled insulating state, with a positive value above half-filling and a negative value below half-filling. This Hall measurement demonstrates that the metallic states inside the halo are closely related to the half-filled insulator, probably by a change of Fermi level from half-filling to the inside of the subband (Extended Data Fig. 2c). Given that the half-filled insulator is spin polarized, the metallic states are probably a ferromagnetic metal, which contains two spin-polarized bands that are shifted in energy by the ferromagnetic exchange coupling ((2) in Extended Data Fig. 2c). Outside the halo, the Hall effect follows the expectation of a single-particle moiré band without correlation effects such as in large-angle TBG, indicating that the system recovers to a normal metallic state.

In Extended Data Fig. 2a, we also notice that a three-quarter-filled insulating state appears on the border of the halo. The simplest possible candidate of this state is a spin- and valley-polarized state. However, within a simple mean-field picture, we expect the lowest-lying excitations in this state to be associated with valley-flip rather than spin-flip as the spin exchange coupling is expected to be larger than the valley exchange splitting²³. This naive picture appears to be inconsistent with the enhancement of the gap by the in-plane magnetic field shown in Fig. 2d in the main text. In addition, the appearance of the quarter-filling state right at the edge of the halo suggests that a mean-field picture may fail to capture the relevant physics. We leave this question regarding the nature of the quarter-filling state to future theoretical works.

Magnetic-field-induced Chern insulator state in the 1.26° sample

In the $\theta = 1.26^\circ$ sample, we observed distinctly different behaviour of the Hall resistance. Under a small perpendicular magnetic field, the Hall resistance is always positive inside the halo (Extended Data Fig. 3b), rather than changing signs across half-filling. The absent sign change of the Hall signal across half-filling may be due to thermal excited carriers of both types as a result of the small insulating gap. It could also be due to the Chern insulator behaviour discussed below. Measuring the Hall resistance with changing magnetic field and density at a fixed displacement field (Extended Data Fig. 3d) reveals a single line of large Hall signal tracing to half-filling with a slope corresponding to $\nu = 4$. At the same time, longitudinal resistance develops a minimum along the same line (Extended Data Fig. 3c). Following the $\nu = 4$ line (black guiding lines in Extended Data Fig. 3c, d), Extended Data Fig. 3e shows the Hall resistance reaches close to a quantized value of $h/4e^2$ when the perpendicular magnetic field $B_\perp > 3 \text{ T}$.

The fact that a single Hall plateau emerges from half-filling strongly suggests that this is not a normal quantum Hall state. Instead, the data highly resemble the Chern insulator shown in MA-TBG¹⁷. Indeed, our theory predicts that in TDBG, the first conduction band has a Chern number $C = 2$ in one valley and an opposite Chern number $C = -2$ in the other valley²³. As shown in the main text, without a perpendicular magnetic field, the half-filled state is spin polarized and valley unpolarized, giving a total Chern number of 0. However, a perpendicular magnetic field couples to the valley degree of freedom through the orbital valley Zeeman effect. When the spin-polarized gap is small such as in the 1.26° device, the valley Zeeman energy can overcome the spontaneous spin-polarized gap and converts the spin-polarized half-filled insulating state into a valley-polarized Chern insulator. Using the valley Zeeman factor from a scanning tunnelling microscopy study and calculation²³, we estimate that valley Zeeman energy surpasses the 0.3 meV gap at a perpendicular field of 0.2 T. This valley-polarized half-filled state fills

two moiré bands (of spin up and spin down) in one valley, adding up to a total Chern number of four.

Critical transition behaviours in the $\theta = 1.26^\circ$ sample

In Extended Data Fig. 4c, the dome of the superconducting-like state, similar to MA-TBG, can be seen next to the half-filled insulator. In addition, cutting through a constant density line, a similar dome structure is visible over the displacement field axis (Extended Data Fig. 4b). The dome in the displacement field terminates on the boundary of the halo. It may first appear that the low-resistance state outside the halo boundary resembles a superconductor as well. However, as we discussed in the main text, there is no critical transition outside the halo. In addition, the I - V characteristic outside the halo is very different from that inside the halo. Within the halo, differential resistance shows a critical current that reduces to zero when approaching the halo boundary (Extended Data Fig. 4f). Outside the halo, in contrast, the I - V characteristic does not fit that of a superconductor (Extended Data Fig. 4g). We believe the low resistance outside the halo is purely caused by ballistic transport. Extended Data Fig. 4d shows that the superconducting-like state has a critical perpendicular magnetic field of about 0.1 T.

In a recent study³¹, He et al. observed a sudden drop of resistance with a residue resistance of about 1 k Ω , similar to our 1.32 $^\circ$ device. They also reported a nonlinear I - V curve, where dV/dI gradually increases with current in a parabolic manner up to a factor of two without signs of critical current. This observation is in stark contrast to the data from our superconducting-like sample, where dV/dI reaches zero at zero bias and saturates to a finite value above the critical current. In their paper, He et al. explain this nonlinear I - V as an effect from the temperature increase due to bias current heating. While this argument can explain the nonlinear I - V observed in their sample with large residue resistance, we demonstrate that our superconductor-like nonlinear I - V is unlikely caused by heating.

At 2 K, the zero-bias resistivity of the sample is close to zero. If we assume the sample is metallic, we can translate resistivity to thermal conductivity. Taking the upper bound of resistivity to be 50 Ω , it converts to 1 nW K⁻¹ in heat conductivity according to the Wiedemann-Franz law at 2 K. From the I - V curve shown in Fig. 3c, we can extract the heating power to be about 13 pW at the critical current of about 300 nA. As a result, the temperature increase is about 13 mK. In contrast, it requires a 5 K temperature increase to bring the sample resistance to the normal value (Fig. 3b). This provides additional confirmation that our observed nonlinear I - V is probably an intrinsic property of the device rather than a heating effect.

Enhancement of the transition temperature with B_{\parallel}

If the superconducting-like behaviour in the 1.26 $^\circ$ sample is indeed from superconductivity, the parallel field dependence shown below suggests that it might be an exotic spin-polarized superconductor. Here we investigate the behaviour of $\rho(T)$ as a function of B_{\parallel} . Extended Data Fig. 5a shows a superconducting dome in the (n, B_{\parallel}) plane with a maximum critical parallel magnetic field $B_{\parallel}^c \approx 1$ T. The salient experimental feature is the B_{\parallel} dependence of the superconducting state below the critical field B_{\parallel}^c . Extended Data Fig. 5b shows ρ at optimal density and displacement field (n_m, D_m) as a function of T and B_{\parallel} . In this optimal superconducting state, ρ vanishes critically as T and B_{\parallel} decreases. We use a phenomenological definition of the critical temperature $T_{50\%}$ defined as the 50% transition point. Interestingly, $T_{50\%}(B_{\parallel})$ follows a non-monotonic behaviour. In particular, $T_{50\%}$ increases as B_{\parallel} increases from 0 to about 0.3 T before it decreases for $B_{\parallel} > 0.3$ T. We also performed I - V characterization at the optimal gate configuration (n_m, D_m) as a function of B_{\parallel} and T to obtain T_{BKT} (Extended Data Fig. 4e). Similar to $T_{50\%}$ above, $T_{\text{BKT}}(B_{\parallel})$ also shows a non-monotonic behaviour as shown in Extended Data Fig. 5b (black circles). These sets of evidence suggest that a small B_{\parallel} can strengthen the superconductivity.

The increase of critical temperature with B_{\parallel} suggests that the Cooper pairs responsible for the superconductivity here, if confirmed, are likely to be spin polarized. One possible scenario for such a state is illustrated in Extended Data Fig. 5d, where the Cooper pairs form between Fermi surfaces with the same spin (spin-triplet) and opposite valleys. This model is consistent with our previous discussion of a ferromagnetic metal parent state inside the halo next to the half-filled insulator, where the Fermi surfaces of two different spins have different filling status. In this spin-polarized pairing scheme, a parallel magnetic field enlarges the majority spin Fermi surface, and strengthens the superconductivity, inducing the change in the critical temperature $\Delta T_c \propto B$ (ref. ²³). The eventual destruction of superconductivity at high magnetic fields can result from the following mechanism. Magnetic flux in between layers leads to a momentum shift, which has an opposite sign in the two valleys, thereby bringing the two pairing Fermi surfaces out of alignment. The latter effect is expected to reduce the critical temperature, $\Delta T_c \propto -B^2$ (ref. ²³). Alternatively, if the ferromagnetic pairing is caused by spin fluctuations, as suggested in the heavy fermion metals³⁷⁻³⁹, a strong parallel magnetic field can suppress the superconductivity by suppressing spin fluctuations⁴⁰.

Meanwhile, in the measurement shown in Extended Data Fig. 5c, we notice that the 0 T resistivity goes slightly negative (about -30 Ω) at the lowest temperature for this specific thermal cycle. In general, we find that the four-terminal resistivity we measure in the 1.26 $^\circ$ device sometimes shows a small residue (-50-50 Ω) that varies between different thermal cycles. The residual resistance is not present in the measurement shown in Fig. 3b. This residual resistance (when it is present in a specific thermal cycle) is sensitive to the measurement configuration. Extended Data Fig. 6 shows two different four-terminal resistance measurement configurations. Between the two configurations (blue curve and red curve), we essentially flip the direction of the current. As we use a low-frequency a.c. (about 17 Hz) for the current source and a lock-in amplifier for the voltage probe, in an ideal condition, we expect to obtain the same signal with opposite polarity. However, we find that the measured signals deviate from this expectation when there is residual resistance at low temperature. Specifically, when flowing current from top to bottom (blue curve in Extended Data Fig. 6), four-terminal resistance is positive, and a positive residual resistance of about 50 Ω remains at the lowest temperature, 2 K. However, when the current is flowing from the bottom to the top (red curve), the four-terminal resistance at higher temperature is negative as expected, but the residual resistance at lower temperature is still positive and is nearly identical to that in the blue curve (see inset).

We believe that the observed anomaly in the residual resistance originates from bias-induced gating in combination with thermoelectric voltages present in our cryostat wiring. Owing to the temperature gradient in the cryostat, a d.c. thermoelectric voltage is always present between different pairs of wires. This d.c. voltage is simply added to the voltage probes on top of the a.c. voltage induced by bias current. In such cases, the a.c. bias voltage on the sample (about half of the bias voltage on the source lead, as the drain is grounded) can modulate the d.c. thermoelectric voltage through a bias-induced gating effect (see ref. ⁴¹ for a similar effect observed in a drag experiment), resulting in a voltage signal synchronizing with the applied a.c. bias current. We can eliminate this bias-induced a.c. gating effect of thermoelectric voltage by subtracting the blue curve from the red curve, where we obtain a near-zero residual resistance within the noise level. During the thermal cycle in obtaining the data in Extended Data Fig. 5c, we did not collect the data in two different configurations, and thus such correction was not possible. Note that this a.c. gating effect becomes appreciable only when the device resistivity is really small (<50 Ω).

Landau fan diagram

In the 1.33 $^\circ$ device under a perpendicular magnetic field, clear fans can be identified coming from the CNP, full fillings $\pm n_i$ (about $\pm 4.1 \times 10^{12}$ cm⁻²)

Article

as well as half-filling $n_s/2$ on the electron-doped side (Extended Data Fig. 7a). The Landau fan from the CNP shows a well-developed quantum Hall sequence with fourfold degeneracy on the valence band side under low magnetic fields, and subsequently develops the full degeneracy-lifted quantum Hall states under higher magnetic fields. The Landau fans on the conduction band side ($n > 0$) are highly unusual. The fan from the CNP shows a sequence of only odd filling fractions $\nu = 3$ and 5. Although the fan coming from the correlated insulating state at half-filling shows a degeneracy of two, consistent with the picture of a spin-polarized half-filled band, the sequence is also of odd numbers $\nu = 3, 5$ and 7. The odd-integer sequenced quantum Hall effect from the half-filling gap may relate to a Berry phase effect on the Landau level, similar to the quantum Hall effect in monolayer graphene. Theory²³ predicts that the isolated flat conduction band (c_1) in TDBG carries non-trivial Berry curvature and a non-zero Chern number. It is then possible that the Berry curvature accumulates to a π or 3π phase on certain Landau orbits, resulting in a quantum Hall filling fraction sequence of $2(N - 1/2)$ or $2(N - 3/2)$, with integer N .

There is also a single quantum Hall state $\nu = 3$ projected down to the quarter-filled conduction band. This state could be a magnetic-field-induced Chern insulator, similar to the $\nu = 4$ Chern insulator in 1.26° device discussed above. As this fan projects down to quarter-filling, it is likely that both spin and valley are polarized. We note that the valley Chern number corresponding to this specific state is $C = 3$, although $C = 2$ is generally expected²³. Further study is required to clarify these experimental observations. Above a perpendicular magnetic field of 7 T, the half-filled insulator disappears, presumably due to the orbital effect of the perpendicular magnetic field.

The fan diagram of the 1.26° device is also intriguing. Besides the Landau fans, we point out there is an obvious oscillation of longitudinal resistance around $n = -n_s/2$ that does not sensitively depend on doping (horizontal features marked in Extended Data Fig. 7b). These oscillations are not from quantum Hall states, but from Hofstadter's butterfly. They are a result of the interplay between two different periodicities in the system: moiré superlattice and magnetic length. When one moiré superlattice contains $1/N$ magnetic flux (N is an integer), the two length scales become commensurate and produces a minimum in resistivity. These features are indicative of a highly uniform twisting angle distribution in the sample. We use these features to determine the twist angle in this device.

Effective mass of the $\theta = 1.33^\circ$ and $\theta = 1.26^\circ$ samples

We calculate the effective cyclotron mass from temperature-dependent magnetoresistance (Shubnikov–de Haas (SdH)) oscillations. The cyclotron mass is a measure of the density of states and thus directly related to the Landau-level separation (cyclotron gap) under a given magnetic field. As temperature increases, the SdH oscillation amplitude is reduced following $\Delta R \propto \chi/\sinh(\chi)$, where $\chi = \frac{2\pi^2 k m^* T}{\hbar e B}$.

For the $\theta = 1.33^\circ$ sample, we measured SdH oscillations at all densities between filling factor $n/n_s = -1$ and 1, at $T = 0.3, 2, 3, 4, 6, 9$ and 14 K (example: Extended Data Fig. 8a–c). We then extracted the oscillation amplitudes and plotted them as a function of T/B . Fitting $\Delta R(T/B)$ with the above formula with m^* being the only fitting parameter, we obtained the effective cyclotron mass shown in the main text. Similarly, we measured SdH oscillations for the $\theta = 1.26^\circ$ sample and extracted an effective mass $m^* = 0.23m_e$, as shown in Extended Data Fig. 8e, f.

Device fabrication and characterization

All the devices presented in this study were prepared using the dry transfer method⁴², using stamps consisting of polypropylene carbonate film and polydimethylsiloxane. Half of a bilayer graphene flake was torn and picked up by a stack of graphite/hBN on the transfer stamp. Then the remaining bilayer graphene flake on the substrate was rotated by the desired angle and picked up. The stacks were deposited on a

300-nm SiO₂/Si substrate after picking up the rest of hBN and graphite layers. Part of the bilayer graphene flakes was extended outside the hBN area onto polypropylene carbonate to prevent the graphene from freely rotating on the hBN. The resulting stacks were fabricated into 1–2- μm -wide devices to ensure a uniform twist angle in the relatively narrow channel. The temperature of the stack was always kept below 180 °C during the stacking and fabrication processes.

We measured a total of seven devices with different twist angles in this study. All samples were encapsulated by the hBN layers. In the 1.32°, 1.33°, 1.41°, 1.53° and 2.00° devices, both the top and bottom gates were made from graphite. The 1.26° device utilized a graphite top gate and a heavily doped silicon bottom gate below the hBN substrate and 300-nm SiO₂ dielectric. The 1.48° device used a silicon bottom gate and a metal top gate. Most of the devices were fabricated into Hall bars with the exception of the 1.26° and 1.41° samples, which were fabricated into a Van der Pauw geometry. The gate configurations and device images are shown in Extended Data Fig. 9.

The resistivity presented here was measured at 17.7 Hz using the standard lock-in technique, with a 0.5–1.0 mV voltage bias and a current-limiting-resistor of 100 k Ω connected in series with the sample, which limits the current in the sample to an upper bound of 5–10 nA. This bias scheme is to ensure neither the voltage nor the current becomes too large when sweeping across states with drastically different resistance (insulators or superconducting-like states). The four-terminal voltage and the source–drain current are measured simultaneously with two lock-in amplifiers to obtain the four-terminal resistance. Resistivity is then obtained by multiplying the resistance by a geometric factor (about 4.5 for Van der Pauw devices).

Figure 1f and Extended Data Fig. 9a, c–g show large-scale gate scans of the longitudinal resistivity in all samples. These samples show insulating states at full filling under the zero displacement field and at the CNP under a large displacement field. Moreover, in particular, the 1.32°, 1.48°, 1.53° and 2.00° devices show a CNP gap under the zero displacement field, which closes and reopens with increasing displacement field. For the 1.32° device, we note that the gate scan diagram shows a wide insulating region at full filling and double peaks at half-filling, suggesting that there is additional moiré periodicity in the channel other than 1.32°. The CNP gap in the 1.32° device under zero displacement field probably originated from the larger twist angle region of the sample, as none of the neighbouring angle devices (1.26°, 1.33°, 1.41°) has a gap at the CNP under zero displacement field. We remark that theory²³ predicts a gap at the CNP opens up even at zero displacement field when $\theta > 1.5^\circ$, qualitatively agreeing with our experimental observation.

The twist angles are estimated from two independent methods. For the first method, we measure the gate voltages of full-filling gaps and convert these voltages to full-filling density n_s using the gate capacitance. The gate capacitance used for this conversion is calibrated by Landau fan diagrams. We then calculate the twist angle from the fact that full filling corresponds to four electrons per moiré unit cell so the moiré unit cell area $A = 4/n_s$. The main source of errors for this method is in locating the exact position of full filling in the gate voltage. We also use the radiating Landau fan coming from full filling to help locate its exact position. Typically, we can identify the position of full filling to an accuracy of $\delta n_s \approx 10^{11} \text{ cm}^{-2}$, corresponding to a twist angle error of $\pm 0.02^\circ$. The second method exploits Hofstadter's butterfly features under magnetic fields. Here we find carrier-density-independent oscillations of the longitudinal resistance R_{xx} under perpendicular magnetic fields, with the minimum of R_{xx} appearing when the magnetic flux in a moiré unit cell is a fraction of the flux quantum, $BA = \phi_0/N$ (Extended Data Fig. 7b), where B is magnetic field, ϕ_0 is the flux quantum and N is an integer. These features are used to calculate the twist angle with even better accuracy ($\pm 0.01^\circ$).

In Extended Data Fig. 9a, we observe negative resistivity in a part of the 2D gate scan. These anomalous signals can be attributed to

non-transparent contacts in these gate regions. Comparing with the 2D map of the two-terminal resistance measured in this device (Extended Data Fig. 9b), we find that the gate regions where negative resistivity were observed in Extended Data Fig. 9a in general correspond to the gate regions where a large contact resistance is demonstrated by the two-terminal measurement. This strong correlation between the apparent 'negative' four-terminal resistivity and high contact resistance suggests that the negative four-terminal resistivity originates from inefficient contact equilibration in these gate regimes. Indeed, the contact transparency can be hindered by the unintended p-n junction formation near the metal contacts when the applied gate voltages conspire with the work function mismatch between graphene and metal to cause an accumulation of the opposite polarity of charges near the contact and in the channel. However, near the half-filled insulator region, where most of our research is focused, the two-terminal resistance stays less than 10 k Ω , demonstrating excellent contact transparency. Thus, we conclude that the contact anomaly can be excluded as a possible cause of our experimental observation near the correlated insulator regime. We also notice that the correlated insulating state in the positive displacement field side ($V_{TG} < 0$ and $V_{BG} > 0$) shows a much weaker signature than the negative displacement field side. The absence of a clear signature of correlated insulator on the opposite side of the displacement field is also likely due to the inefficient contact equilibration in these particular gate configurations, as shown in Extended Data Fig. 9b.

Data availability

The data that support the findings of this study are available from the corresponding author upon reasonable request.

35. Jung, J. & MacDonald, A. H. Accurate tight-binding models for the π bands of bilayer graphene. *Phys. Rev. B* **89**, 035405 (2014).
36. Moon, P. & Koshino, M. Optical absorption in twisted bilayer graphene. *Phys. Rev. B* **87**, 205404 (2013).
37. Saxena, S. S. et al. Superconductivity on the border of itinerant-electron ferromagnetism in UGe₂. *Nature* **406**, 587–592 (2000).
38. Aoki, D. et al. Coexistence of superconductivity and ferromagnetism in URhGe. *Nature* **413**, 613–616 (2001).
39. Huy, N. T. et al. Superconductivity on the border of weak itinerant ferromagnetism in UCoGe. *Phys. Rev. Lett.* **99**, 067006 (2007).
40. Julian, S. Viewpoint: pairing with spin fluctuations. *Physics* **5**, 17 (2012).
41. Liu, X. et al. Frictional magneto-Coulomb drag in graphene double-layer heterostructures. *Phys. Rev. Lett.* **119**, 056802 (2017).
42. Wang, L. et al. One-dimensional electrical contact to a two-dimensional material. *Science* **342**, 614–617 (2013).

Acknowledgements The major experimental work is supported by DOE (DE-SC0012260). P.K. acknowledges support from the DoD Vannevar Bush Faculty Fellowship N00014-18-1-2877. Z.H. is supported by ARO MURI (W911NF-14-1-0247). A.V., J.Y.L. and E.K. were supported by a Simons Investigator Fellowship. K.W. and T.T. acknowledge support from the Elemental Strategy Initiative conducted by the MEXT, Japan, A3 Foresight by JSPS and the CREST (JPMJCR15F3), JST. A portion of this work was performed at the National High Magnetic Field Laboratory, which is supported by the National Science Foundation Cooperative Agreement Number DMR-1157490* and the State of Florida. Nanofabrication was performed at the Center for Nanoscale Systems at Harvard, supported in part by an NSF NNIN award ECS-00335765. We thank S. Fang, S. Carr, Y. Xie, E. Kaxiras, B. I. Halperin, A. F. Young, J. Waissman and A. Zimmerman for helpful discussion.

Author contributions X.L. and P.K. conceived the experiment. X.L., Z.H., Y.R., H.Y. and D.H.N. fabricated the samples. X.L. and Z.H. performed the measurements and analysed the data. E.K., J.Y.L. and A.V. conducted the theoretical analysis. X.L., Z.H. and P.K. wrote the paper with input from Y.R., H.Y., E.K., J.Y.L. and A.V. K.W. and T.T. supplied hBN crystals.

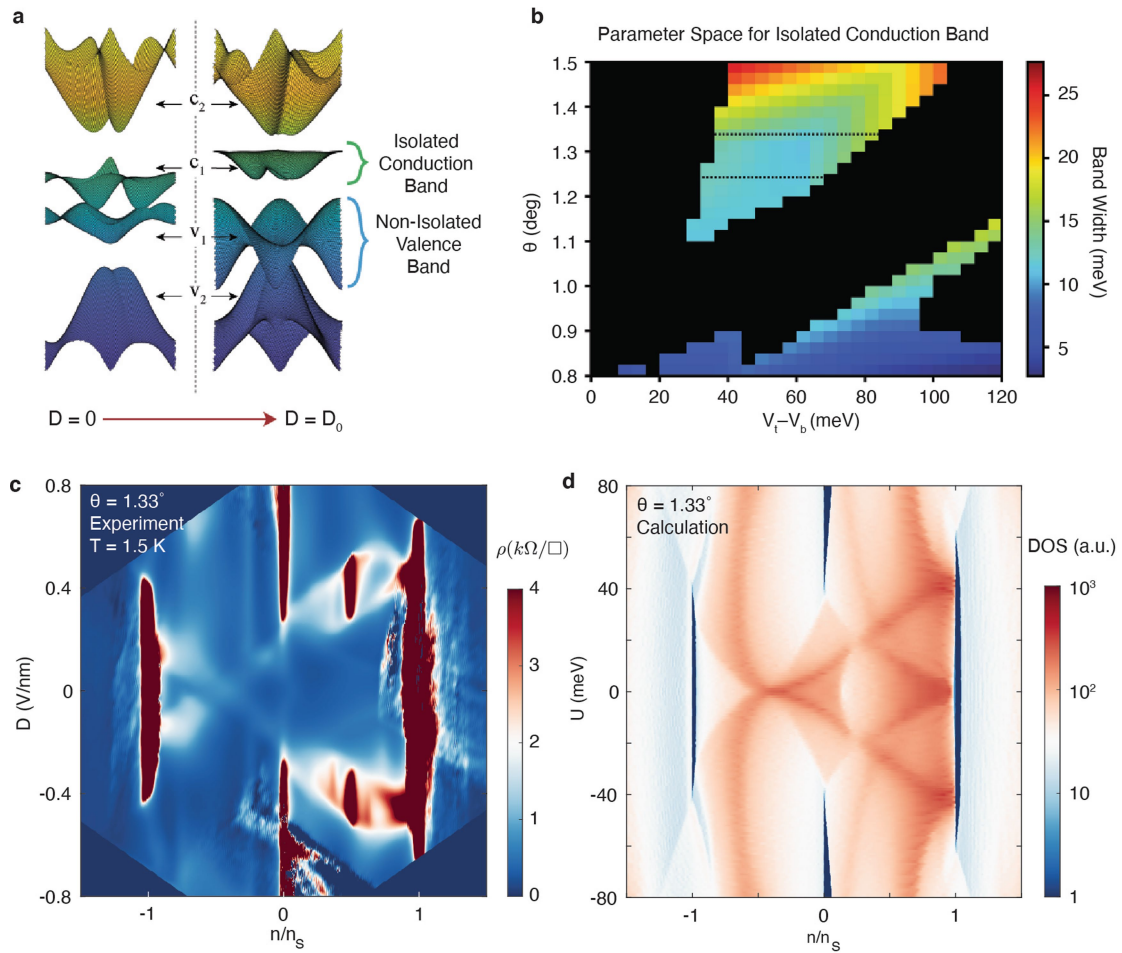
Competing interests The authors declare no competing interests.

Additional information

Correspondence and requests for materials should be addressed to X.L. or P.K.

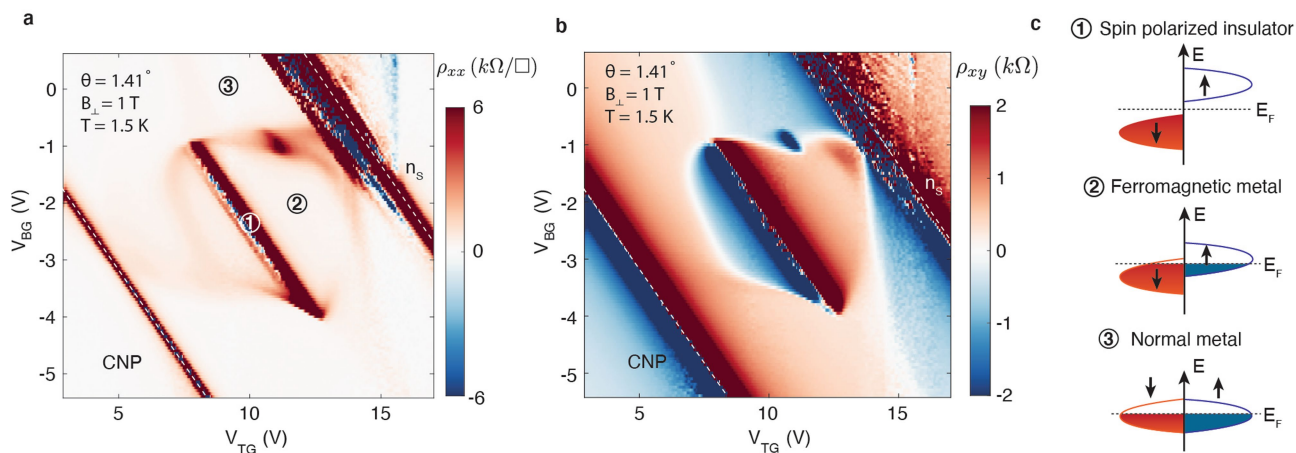
Peer review information *Nature* thanks Hu-Jong Lee, Ming-Hao Liu and the other, anonymous, reviewer(s) for their contribution to the peer review of this work.

Reprints and permissions information is available at <http://www.nature.com/reprints>.



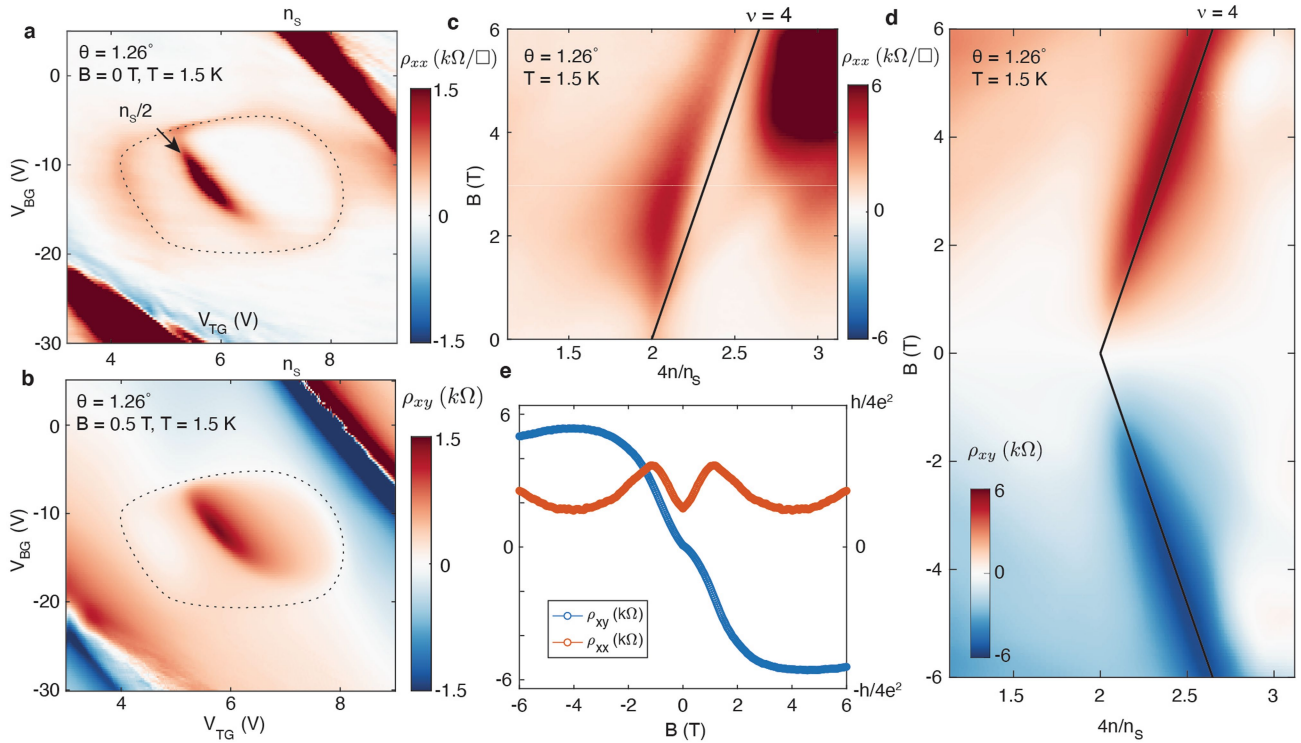
Extended Data Fig. 1 | Theoretical band structure of TDBG. a, Calculated band structure of TDBG at zero displacement field and optimal displacement field D_0 for the isolated flat band. **b**, Calculated parameter space for isolated conduction band (x axis is onsite potential difference $U = V_t - V_b$ between the top and bottom graphene layer, y axis is twist angle). Colour represents the bandwidth of the first conduction band c_1 (meV). In the coloured parameter space, c_1 is isolated from the second conduction band and the first valence bands. The two dotted lines represent cuts at $\theta = 1.26^\circ$ and $\theta = 1.33^\circ$. **c**, Resistivity

as a function of filling fraction and displacement field in the $\theta = 1.33^\circ$ sample. A cross-like feature of high resistivity is formed along two lines from $(n, D) = (1, -0.2)$ to $(1, 0.6)$ and $(-1, 0.2)$ to $(-1, -0.6)$, passing through the half-filled insulating states. **d**, Density of states at the Fermi energy calculated by the continuum model. The single-particle insulators ($n/n_s = 0, \pm 1$) in experiment match well with the gaps shown in the calculation and the van Hove singularity captures the cross-like pattern in experiment.



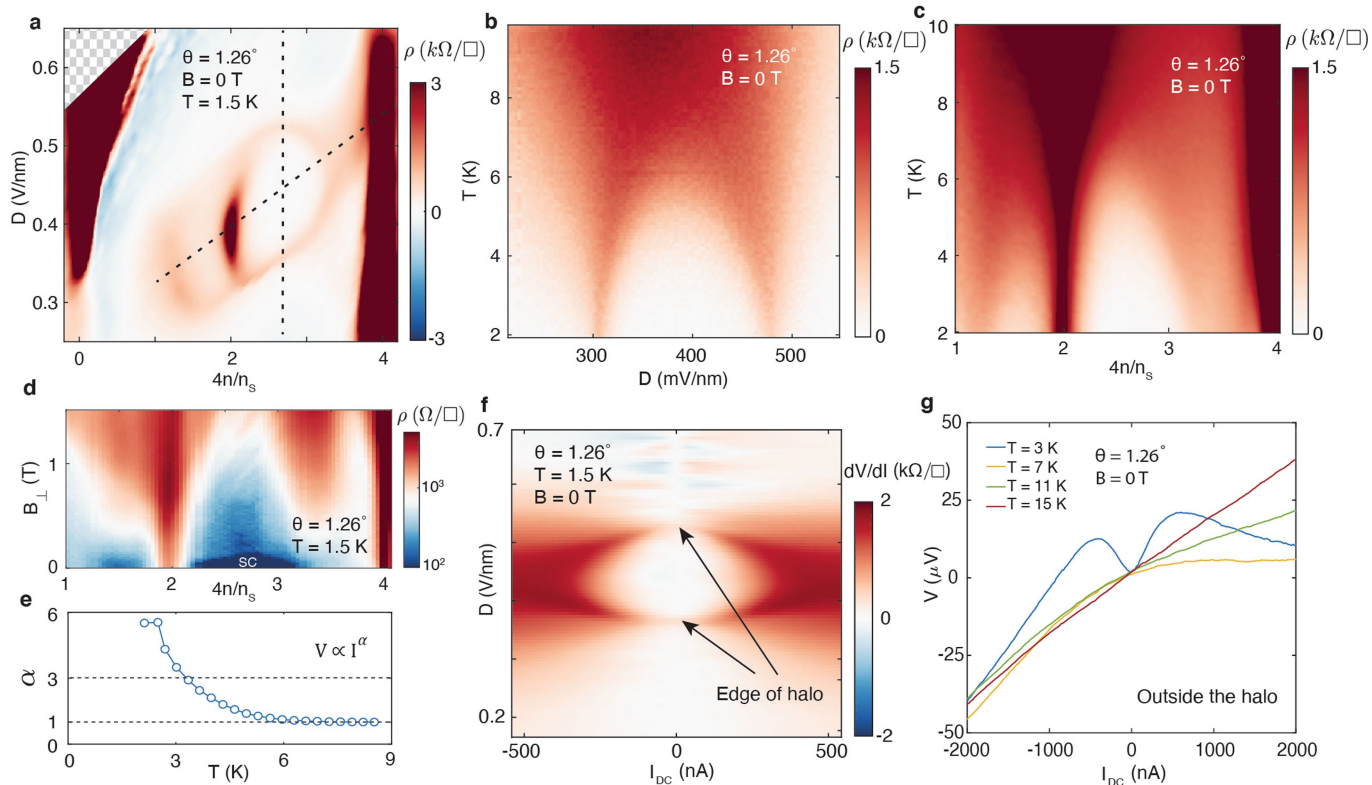
Extended Data Fig. 2 | Hall effect in a device with robust half-filled insulators. a, b, Longitudinal resistivity (a) and Hall resistance (b) of the $\theta = 1.41^\circ$ device around half-filling at $T = 1.5 \text{ K}$ and under perpendicular magnetic field $B_{\perp} = 1 \text{ T}$. Data are symmetrized between positive and negative fields to eliminate mixing. The halo structure is apparent around the half-filled insulator and a three-quarter-filled insulating state resides on the border of the halo.

The Hall resistance changes sign across the half-filled insulator inside the halo. c, Illustration of electron orders for different regimes. The left half (right half) of the cartoon represents the band of spin down (up) electrons. For half-filling, only one species of spin is filled. Inside the halo, one spin species is populated more than the other. Outside the halo, both spins are equally populated.



Extended Data Fig. 3 | Field-induced Chern insulator in the $\theta=1.26^\circ$ device. **a, b**, Longitudinal resistivity at $B=0$ (a) and Hall resistance at $B_{\perp}=0.5$ T (b) in the $\theta=1.26^\circ$ sample at $T=1.5$ K. The Hall resistance here is symmetrized with both directions of the magnetic field. **c, d**, Fan diagram of longitudinal resistivity (c)

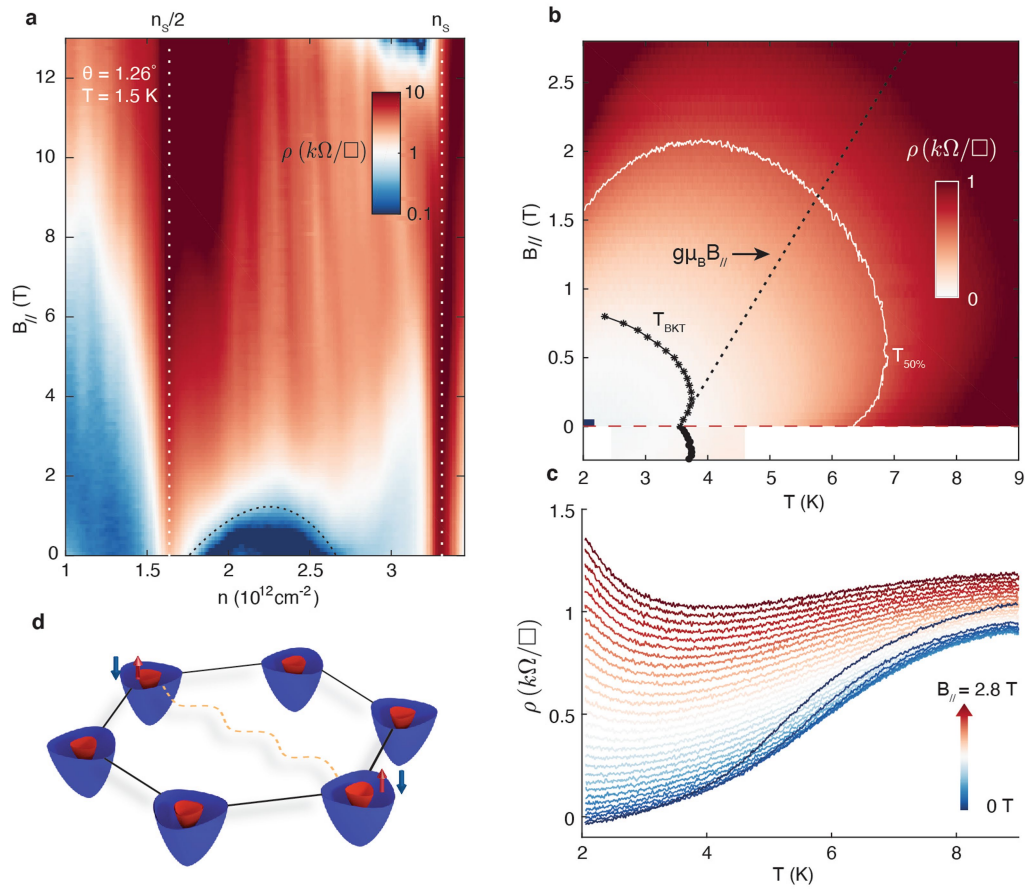
and Hall resistance (d) at $T=1.5$ K at a constant displacement field. The black line marks the expected position for $\nu=4$ Chern insulator state originating from half-filling. **e**, Longitudinal resistivity and Hall resistance along the black line shown in c and d.



Extended Data Fig. 4 | Critical behaviours in the $\theta = 1.26^\circ$ device.

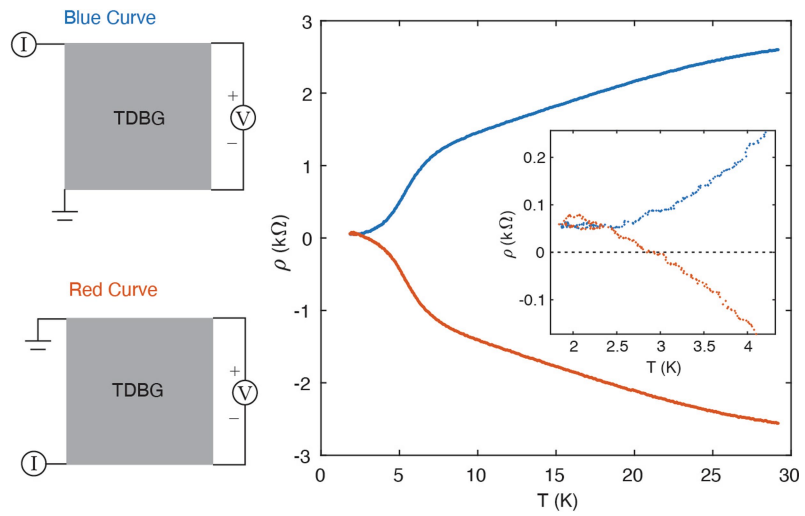
a, Resistivity in 1.26° device plotted against filling factor and displacement field. **b**, Resistivity as a function of displacement field and temperature along the constant density line shown in **a**. **c**, Resistivity as a function of filling and temperature along the tilted line in **a**. The dome of the low resistance state can be seen next to the half-filled insulator. **d**, Resistivity on a log scale as a function

of filling and perpendicular magnetic field. **e**, The power α in $V \propto I^\alpha$ as a function of temperature from fitting the top left inset of Fig. 3c. $\alpha = 3$ is defined as the BKT transition temperature. **f**, Differential resistance as a function of current and displacement field along the constant density line shown in **a**. **g**, I - V curves outside the halo.

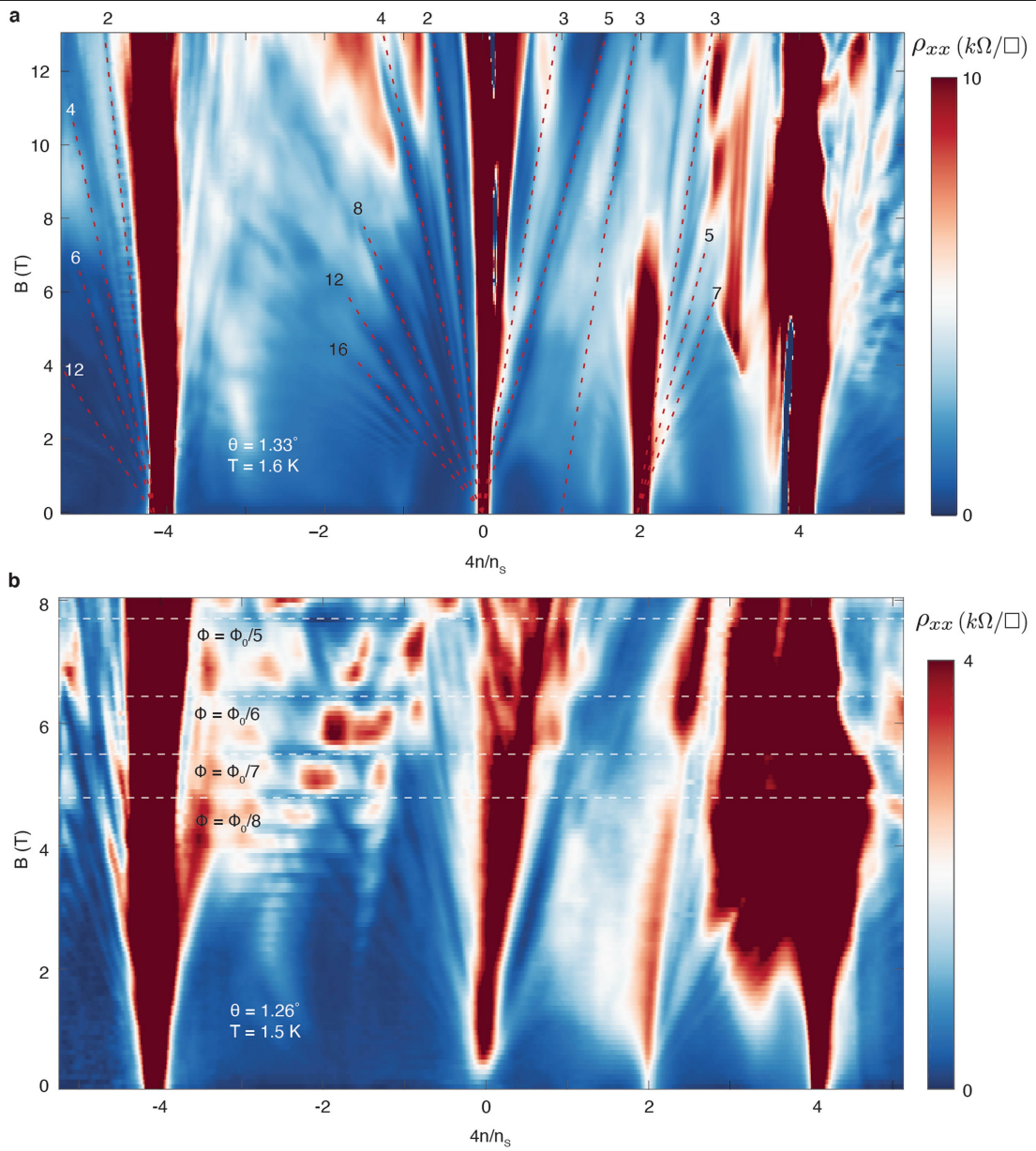


Extended Data Fig. 5 | Enhancement of the critical temperature under in-plane magnetic field. **a**, Resistivity as a function of in-plane magnetic field across the half-filled insulator and superconducting-like state in the 1.26° device. **b**, Resistivity as a function of temperature and in-plane magnetic field at optimal doping and displacement field. T_{BKT} denotes the BKT temperature extracted from nonlinear IV measurements. $T_{50\%}$ marks the temperature where

resistance is half of the normal resistance. **c**, Line traces at different in-plane magnetic fields. **d**, Illustration of pairing in spin-polarized superconductor. The blue (red) surface represents the spin down (up) electron band. The two bands are filled differently due to the parent ferromagnetic metallic state. The hexagon represents the Brillouin zone of graphene lattice. Pairing thus happens between Fermi surfaces of the same spin and opposite valleys.

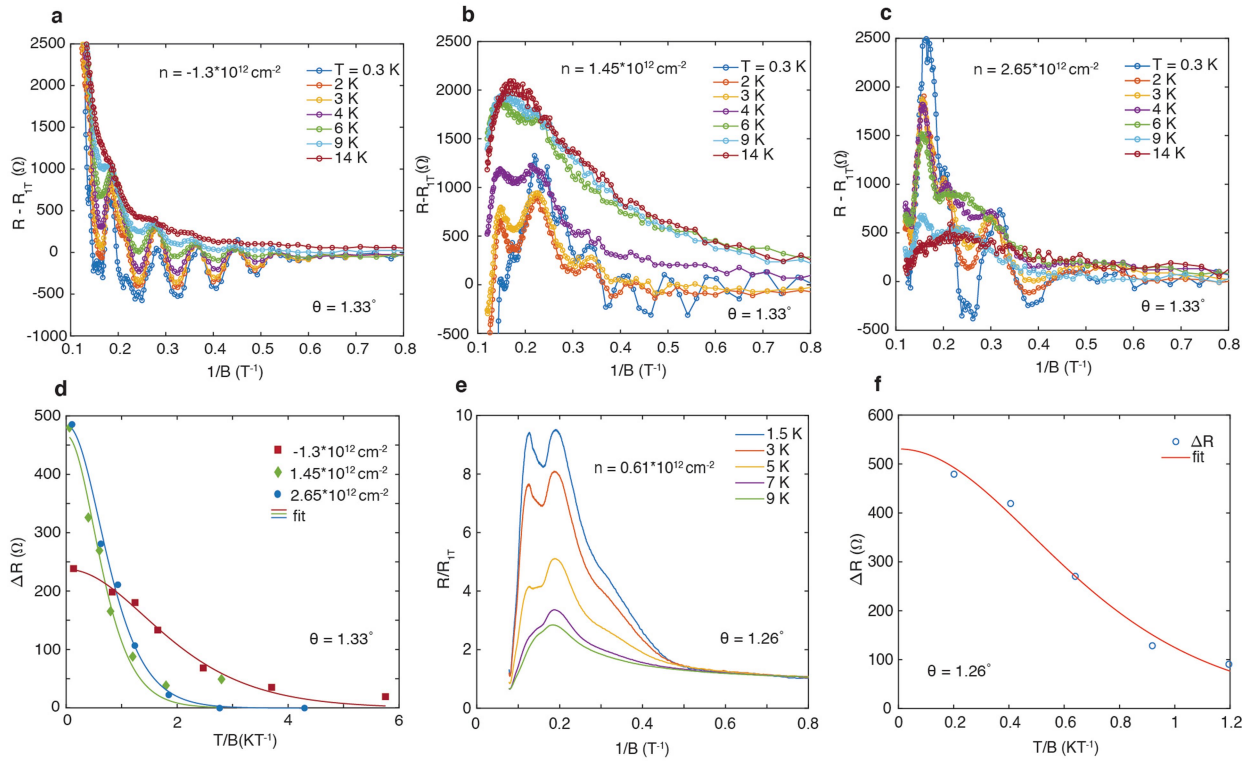


Extended Data Fig. 6 | Origin of a small residual resistivity at $T \ll T_c$. $R(T)$ curve measured in the superconducting regime of the 1.26° device in two measurement configurations. The voltage probes are kept the same between the two configurations while the source and the drain contacts are switched.



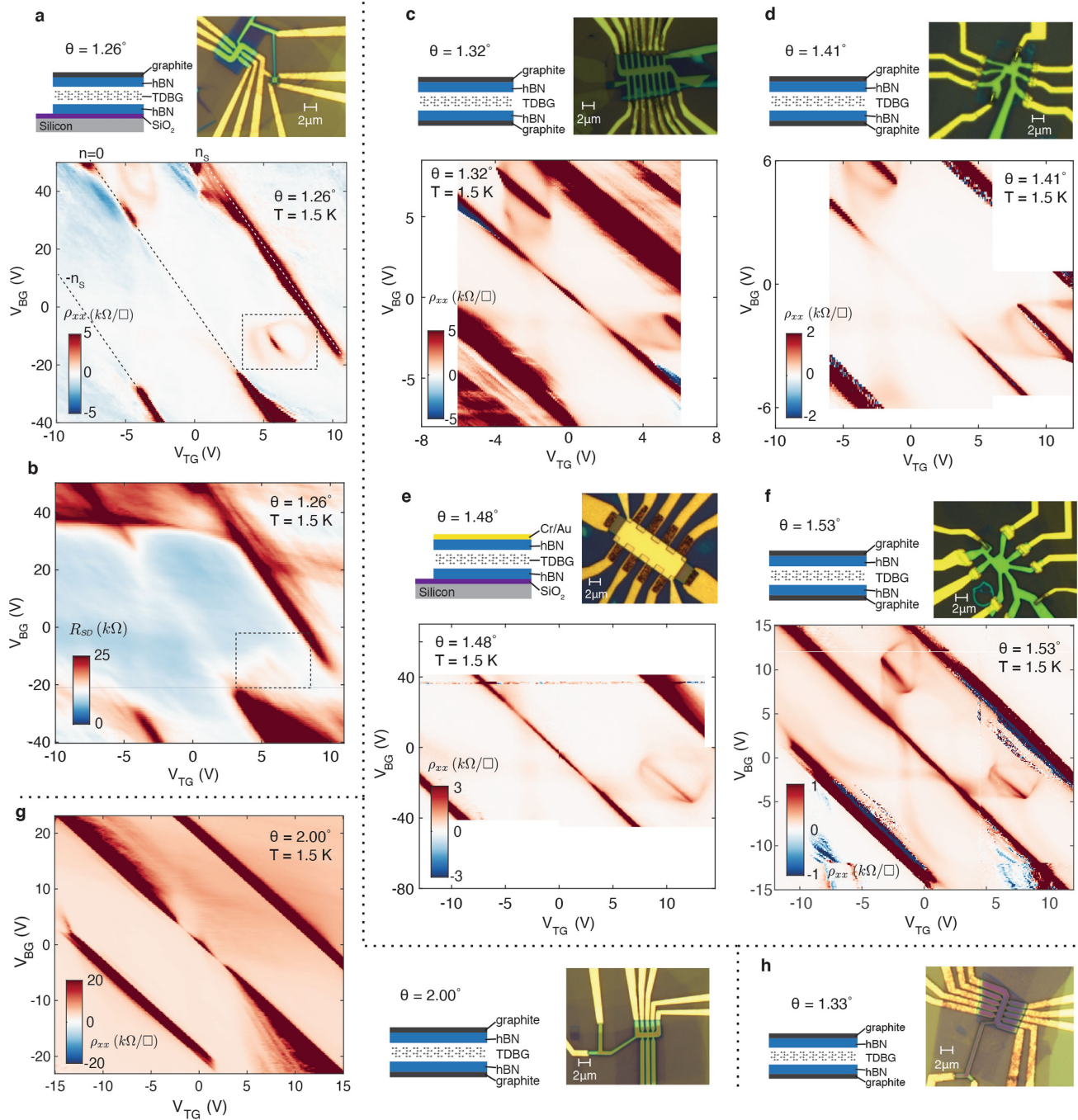
Extended Data Fig. 7 | Landau fan diagram as a function of filling fraction and perpendicular magnetic field. a, The 1.33° device. The numbers next to the guiding lines indicate Landau-level filling factors. **b,** The 1.26° device.

Horizontal lines highlight the Hofstadter's butterfly features that occur when a simple fraction of the flux quantum ϕ_0/N (N is an integer) penetrates through a moiré unit cell.



Extended Data Fig. 8 | Effective mass calculation for the 1.33° and 1.26° devices. **a–c**, Temperature-dependent SdH oscillations in the $\theta = 1.33^\circ$ device at a few representative density points: $n = -1.3 \times 10^{12} \text{ cm}^{-2}$ (**a**), $1.45 \times 10^{12} \text{ cm}^{-2}$ (**b**) and $2.65 \times 10^{12} \text{ cm}^{-2}$ (**c**). **d**, Extracted oscillation amplitudes as a function of T/B

for the density configuration shown in **a–c** and corresponding fitting curves. **e**, Temperature-dependent SdH oscillations in the $\theta = 1.26^\circ$ device at $n = 0.61 \times 10^{12} \text{ cm}^{-2}$, which is above half-filling and inside the halo. **f**, Extracted oscillation amplitudes as a function of T/B in the $\theta = 1.26^\circ$ device.



Extended Data Fig. 9 | Device characterization. **a, c–g**, Device structure, optical image and four-terminal resistivity map of each device: 1.26° (**a**), 1.32° (**c**), 1.41° (**d**), 1.48° (**e**), 1.53° (**f**) and 2.00° (**g**). For the 1.26° device, the active device is the four-terminal Van der Pauw sample. The structure of each

device is depicted by the cross-section illustration on the left of the optical image. **b**, Two-terminal resistance measured in the 1.26° device in the same gate voltage range presented in **a**. Dashed square marks the active area studied. **h**, Structure and optical image of the 1.33° device.

Extended Data Table 1 | Summary of all TDBG devices studied

θ	1.26°	1.32°	1.33°	1.41°	1.48°	1.53°	2.00°
w (meV)	12 (11)	13	13 (10)	17	21	24	71
$\Delta_{n_g/2}$ (meV)	0.30	2.8	3.0	4.2	0.54	0.72	N.A.
ρ_{min} (k Ω/\square)	<0.01	1.04	0.82	0.21	0.28	0.14	N.A.

Minimum bandwidth w at the optimal displacement field obtained from continuum model calculation (experimentally estimated bandwidth is shown in the bracket), half-filled gap $\Delta_{n_g/2}$ and resistivity well below the critical transition inside the halo ρ_{min} for devices with different twist angles. There is no sign of any correlated state in the 2.00° device (N.A.). $\Delta_{n_g/2}$ shows a general trend of diminishing away from the optimal angle 1.41°, although the disorder might cause some device-to-device variation.